metrology

MDPI

Article

Experimental Visualization of Unsteady Flow in a Transonic Oscillating-Blade Compressor Cascade Using High-Speed Two-Wavelength Interferometry

Jindřich Hála [1,*], Pavel Psota [2], David Šimurda [1] and Jan Lepicovsky [1]

[1] Institute of Thermomechanics, Czech Academy of Sciences, 182 00 Prague, Czech Republic; jandrsc@gmail.com (J.L.)
[2] Faculty of Mechatronics, Informatics and Interdisciplinary Studies, Technical University of Liberec, 461 17 Liberec, Czech Republic; pavel.psota@tul.cz
* Correspondence: hala@it.cas.cz

Abstract

This study presents experimental results from high-speed interferometric measurements on a transonic compressor blade cascade, where three of the five blades were torsionally oscillated at various frequencies up to 150 Hz and different inter-blade phase angles. The primary research objective is to develop and validate a non-intrusive methodology capable of quantifying unsteady flow fields surrounding aeroelastically unstable components. The resulting flow field images demonstrate the potential of the method. Unlike classical interferometric methods, the proposed approach has less stringent requirements for the optical quality of the test section windows. This advantage allows for the use of organic-glass windows, which are necessary for investigating highly loaded compressor blade cascades. Such windows are required to accommodate the suction slots used to maintain a representative Axial Velocity Density Ratio (AVDR). Unlike the classical schlieren technique, the method provides quantitative results with high spatial and temporal resolution, while the synthetic schlieren images can also be produced. The method proved suitable for measurements in the harsh environment of transonic flow through oscillating blades and is capable of capturing important unsteady flow phenomena.

Keywords: unsteady aerodynamics; axial compressor; linear cascade; two-wavelength interferometry

Check for updates

Academic Editors: Han Haitjema and Ki-Nam Joo

Received: 27 March 2026
Revised: 10 June 2026
Accepted: 12 June 2026
Published: 16 June 2026

1. Introduction

Understanding the unsteady aerodynamic phenomena in transonic compressor cascades is crucial for advancing turbomachinery design and performance. This study focuses on the experimental analysis of the unsteady flow field within a linear transonic compressor cascade, specifically examining the effects of oscillating blades on flow dynamics. Building on prior research that used optical measurement techniques to visualize transonic airflow in stationary cascades [1], the present investigation introduces controlled oscillations of three blades within the cascade at varying frequencies and phase shifts. The experiments are conducted at a design inlet Mach number $M_1 \sim 1.09$ and blade oscillation amplitude $\alpha_b = 0.25°$.

Particle image velocimetry (PIV) [2,3] is a standard technique for measuring velocity fields in airflow studies, particularly for low-speed incompressible flows. In high-speed, transonic, or supersonic flows, tracer particles no longer follow the flow streamlines.

Alternative optical methods, such as Schlieren imaging [4,5] and shadowgraphy [6], enable visualization of compressible flow structures. However, these techniques provide primarily qualitative information and do not allow for direct quantitative measurements. In contrast, interferometric methods measure the optical phase integrated along the optical path, which is directly proportional to the fluid density rather than to its spatial derivatives. Consequently, interferometric techniques have proven useful for many applications in experimental fluid mechanics.

In transonic and supersonic flows, the density field often exhibits rapid spatial variations caused by expansion regions, shock waves, and shock–boundary-layer interactions. These phenomena lead to abrupt changes in pressure, temperature, and density, which introduce large phase gradients in interferometric measurements. As a result, standard single-wavelength interferometry suffers from the phase ambiguity problem [7].

The primary gap addressed by this research is the lack of a robust, non-intrusive optical diagnostic capable of delivering full-field quantitative flow parameters under active structural flutter. To overcome this limitation, the use of two wavelengths has been proposed [8]. By employing two coherent sources with different wavelengths, a synthetic wavelength can be generated, effectively extending the unambiguous measurement range compared to single-wavelength interferometry. This concept has been widely applied for measuring steady or slowly varying quantities, such as object topography [8–10]. However, its application to rapidly varying phenomena is more challenging, as both wavelengths must be recorded within a single exposure.

Several off-axis optical configurations have been proposed to address this requirement [11–13]. Nevertheless, when measuring fast phenomena, the use of very short exposure times reduces the total integrated light energy captured by the sensor and increases noise levels, which complicates reliable phase retrieval and data processing.

In the two-wavelength approach, the interference phases corresponding to the individual wavelengths are first retrieved and subsequently used to generate a beat fringe pattern referred to as the synthetic phase. This synthetic phase can be scaled and compared with one of the single-wavelength phase maps. From this comparison, a fringe order map can be obtained, enabling the unwrapping of the single-wavelength phase map. In this way, the measurement range is extended while preserving the accuracy associated with the shorter wavelength.

However, the standard data processing procedure fails when the difference between the synthetic phase and the single-wavelength phase exceeds π radians. This situation frequently occurs in the presence of noise or optical aberrations affecting the phase maps obtained at different wavelengths. Several approaches have been proposed to mitigate this problem, including image-processing techniques such as total variation regularization or region segmentation [14]. These methods can reduce noise but require careful parameter tuning and may not be suitable for all datasets, particularly in the case of undersampled measurements.

Another possibility is the use of multi-wavelength hierarchical unwrapping [15–17]. However, such approaches typically require complex optical arrangements and multiple wavelengths, which increases system complexity and cost and limits their applicability to single-shot measurements of dynamic phenomena.

Consequently, experimental fluid mechanics still lacks a robust interferometric methodology capable of providing highly accurate and reliable measurements of rapidly varying compressible flows with large density gradients under realistic experimental conditions. The method presented in this work addresses this limitation and enables repeatable measurements even in challenging environments.

https://doi.org/10.3390/metrology6020041

In this study, the blade flutter test facility at the Institute of Thermomechanics of the Czech Academy of Sciences, located in the High-Speed Laboratory in Nový Knín, was used [18,19]. The facility comprises a linear cascade with five adjustable blades capable of prescribed oscillatory motions (Figure 1). The blades represent the midsection of a DFVLR transonic compressor stage rotor at 45% of the blade height [20]. The geometrical and design flow parameters of this MCA-type blade cascade are given in Table 1. The central three blades are actuated by high-speed asynchronous electric motor to oscillate at controlled frequencies and phase shifts, allowing for a detailed study of blade movement on the unsteady flow field. The oscillation parameters can be varied and measured using a laser triangulation sensor. Additionally, the middle blade (No.3) is instrumented with seven Kulite high-speed pressure sensors on the suction side mid plane, while the neighbouring blades have static pressure taps on the surface connected to NetScanner 9116 pressure transducer. Static pressure is also measured at multiple locations upstream and downstream of the cascade, while total pressure is measured at the inlet to the test section. The entire test section assembly is mounted in a modular in-draft type, open-circuit wind tunnel (Figure 2).

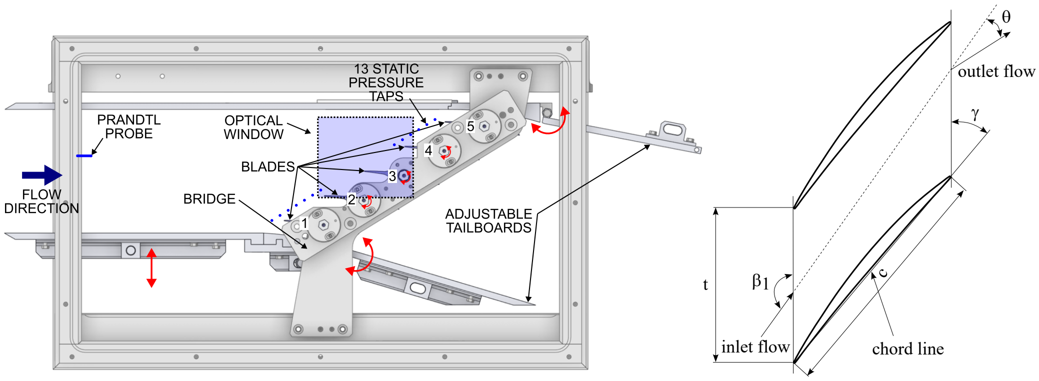

(**a**) (**b**)

Figure 1. Scheme of the test section with 5 transonic compressor blades (**a**) and blade cascade geometry (**b**).

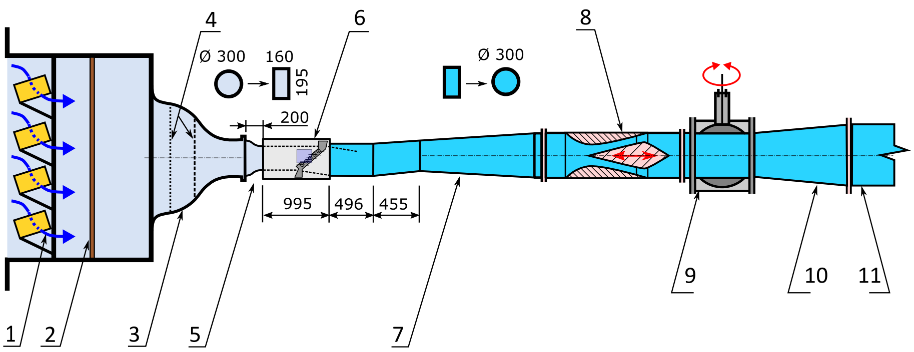

Figure 2. Scheme of the modular wind tunnel: 1—silica-gel dryer, 2—pebble and cloth filter, 3—bell-mouth inlet, 4—honeycomb and screen, 5—contraction and cross-section change, 6—test section, 7—diffuser, 8—control nozzle, 9—quick acting ball valve, 10—diffuser, 11—pipe connection to vacuum chamber.

Table 1. Blade cascade geometry and design parameters.

inlet Mach number M_1	1.09
inlet flow angle β_1	148.5°
flow turning angle θ	12.5°
stagger angle γ	48.5°
pitch-chord ratio t/c	0.621

2. Measurement Techniques

While the fundamentals of single-wavelength (SW) and two-wavelength (TW) interferometry were introduced in Section 1, this section defines the specific mathematical implementation used in this setup. Consider a TW interferometer equipped with two independent laser sources emitting light at wavelengths λ_1 and λ_2. The object waves propagate through the test section along identical optical paths, while the reference waves are adjusted independently. In a single camera exposure, a multiplexed interference pattern is recorded as:

$$I = I_{\lambda_1} + I_{\lambda_2} \tag{1}$$

is recorded, consisting of two independent overlapping interference patterns I_{λ_1} and I_{λ_2} with carrier fringes.

The spectral domain of the multiplexed interferogram I contains a DC term and two conjugate components for each wavelength. The positions of these components can be controlled by adjusting the tilt angles of the reference waves, thereby introducing spatial carrier fringes required for single-shot off-axis Fourier phase reconstruction. The carrier frequencies must be sufficiently high to prevent overlap between the spectral components in the Fourier spectrum while simultaneously satisfying the Nyquist sampling theorem.

After Fourier transformation of the multiplexed interferogram, the first-order spectral sidebands corresponding to the individual wavelengths are extracted using Gaussian band-pass filters. These sidebands contain the complex optical field information required for phase reconstruction. The filter bandwidth determines the spatial resolution of the measurement and consequently also the maximum allowable slope of the reconstructed wavefront phase. Therefore, the bandwidths must be chosen as a compromise between sufficient spectral separation from the DC term and conjugate orders, suppression of spectral overlap, and preservation of high spatial frequencies associated with steep density gradients generated by shock waves and expansion regions.

The interference phases $\Delta\varphi_{\lambda 1}$ and $\Delta\varphi_{\lambda 2}$ are subsequently obtained by inverse Fourier transformation of the filtered complex spectral components. This procedure corresponds to the standard off-axis Fourier-transform phase retrieval method commonly used in digital holography and interferometry.

To extend the range of unambiguity, a beat fringe pattern (synthetic phase map) is generated as

$$\phi(x,y) = \Delta\varphi_{\lambda 2}(x,y) - \Delta\varphi_{\lambda 1}(x,y) \tag{2}$$

The values in Equation (2) are naturally constrained within the interval $(-\pi, \pi]$. However, the corresponding synthetic wavelength

$$\Lambda = \frac{\lambda_1 \lambda_2}{\lambda_2 - \lambda_1} \tag{3}$$

is significantly larger than the individual wavelengths λ_1 and λ_2. According to Equation (3), the range of unambiguity can be adjusted by appropriate selection of wavelengths. Since the uncertainty of interferometric measurements is proportional to the wavelength, the synthetic phase ϕ associated with Λ exhibits higher noise compared to the individual phase

https://doi.org/10.3390/metrology6020041

maps $\Delta\varphi_{\lambda 1}$ and $\Delta\varphi_{\lambda 2}$. Therefore, it is advantageous to combine the large unambiguity range of ϕ with the low uncertainty of the single-wavelength phase map. The standard approach computes the fringe order map

$$N(x,y) = \mathrm{INT}\left[\frac{\Omega(x,y)}{2\pi}\right], \tag{4}$$

where

$$\Omega(x,y) = \phi(x,y)\frac{\Lambda}{\lambda_2} - \Delta\varphi_{\lambda 2}(x,y). \tag{5}$$

In Equation (4), INT denotes rounding to the nearest integer. The phase map $\Delta\varphi_{\lambda 2}$ can then be unwrapped as

$$\Delta\varphi'_{\lambda 2}(x,y) = \Delta\varphi_{\lambda 2}(x,y) + 2\pi N(x,y). \tag{6}$$

The unwrapped phase $\Delta\varphi'_{\lambda 2}$ is no longer restricted to the interval $(-\pi,\pi]$. It retains the low noise level of $\Delta\varphi_{\lambda 2}$ while the range of unambiguity extends to Λ. A key condition for the successful application of this procedure is that the phase error ε introduced in the phase difference must satisfy

$$\varepsilon(\Omega) < \pi. \tag{7}$$

If this condition is violated, the rounding operation in Equation (4) leads to an incorrect fringe order, resulting in erroneous phase unwrapping. To overcome this limitation, a more robust approach can be applied. This method also utilizes the synthetic phase ϕ and phase difference Ω. While ϕ is free of 2π discontinuities, Ω contains many phase jumps because it compares the smooth synthetic phase with the wrapped phase $\Delta\varphi_{\lambda 2}$. The wrapped phase difference is defined as

$$\Omega_W(x,y) = \arg\left\{\exp\left(i\left[\phi(x,y)\frac{\Lambda}{\lambda_2} - \Delta\varphi_{\lambda 2}(x,y)\right]\right)\right\}. \tag{8}$$

In the ideal noise-free case,

$$\mathrm{mod}\left(\phi(x,y)\frac{\Lambda}{\lambda_2}, 2\pi\right) = \mathrm{mod}(\Delta\varphi_{\lambda 2}(x,y), 2\pi). \tag{9}$$

In practical measurements, however, the phase maps are affected by noise, optical aberrations, and phase-reconstruction errors. Therefore, the equality is only approximate and residual phase variations represented by the error term ε remain. Therefore, Ω_W contains no or only a few 2π discontinuities. If Ω_W can be spatially unwrapped (i.e., the gradient of the error satisfies $|\nabla\varepsilon(\Omega)| < \pi$), the phase map $\Delta\varphi_{\lambda 2}$ can be reconstructed as

$$\Delta\varphi'_{\lambda 2}(x,y) = \phi(x,y)\frac{\Lambda}{\lambda_2} - \Omega'_W(x,y), \tag{10}$$

where Ω'_W denotes the spatially unwrapped phase difference [21]. Since both $\phi(x,y)\Lambda/\lambda_2$ and Ω'_W are free of 2π discontinuities, no additional unwrapping errors are introduced provided that the low-density fringe pattern of Ω_W is successfully unwrapped. Consequently, the error criterion is relaxed so that the gradient of the error distribution must satisfy $|\nabla\varepsilon(\Omega)| < \pi$ rather than the absolute error itself. Once the unwrapped interference phase $\Delta\varphi'_{\lambda 2}$ is obtained, it can be used for further physical analysis.

For flow measurements in wind tunnels, the refractive index along the interferometer optical axis is assumed to be constant and the optical phase $\Delta\varphi'_{\lambda 2}(x,y)$ can be related to density distribution $\rho(x,y)$ using

$$\rho(x,y) = \rho_0(x_0,y_0) + \frac{\Delta\varphi'_{\lambda 2}(x,y)\lambda}{2\pi L_T K}, \tag{11}$$

where L_T denotes the wind tunnel test section width, K is the Gladstone-Dale constant and ρ_0 is the reference density located in the position (x_0,y_0) [22].

The interferometric experimental setup is shown in Figure 3. For measurement, a high-speed [23], two-wavelength interferometric technique [21] with an extended range of unambiguity was used. This method employs a high-speed camera to enable short exposure times, effectively avoiding motion blur in the interference patterns and minimizing the influence of environmental disturbances [24]. Fiber optics are used to ensure the compactness and portability of the interferometric system. Quantitative data are obtained in a single shot using the robust TW interferometry.

Two pigtailed diode laser modules (Cobolt series, Hübner Photonics GmbH, Kassel, Germany) operating at wavelengths $\lambda_1 = 550$ nm and $\lambda_2 = 660$ nm were used as coherent light sources. The corresponding synthetic wavelength calculated according to Equation (3) was approximately $\Lambda \approx 3.3$ μm, significantly extending the unambiguous phase measurement range compared to single-wavelength interferometry. Both laser sources were fiber-coupled and combined into the same interferometric arrangement using fiber-optic splitters and ferrules. The use of pigtailed laser modules improved the mechanical stability and compactness of the setup and reduced sensitivity to environmental vibrations.

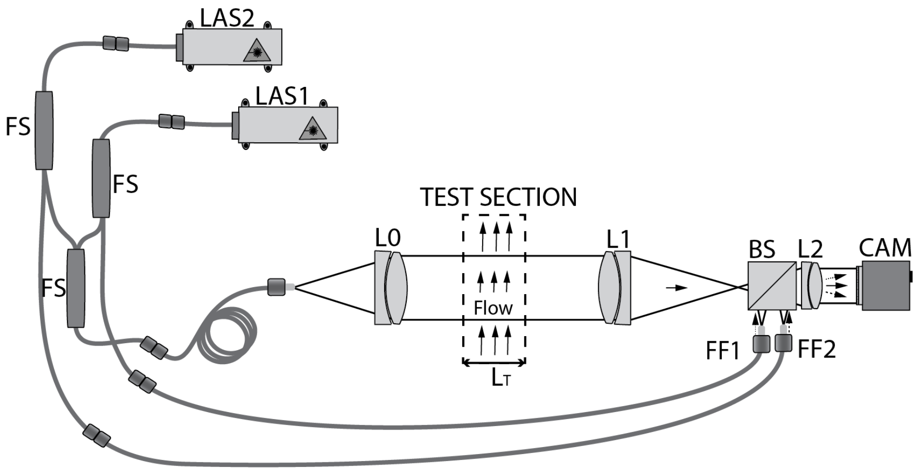

Figure 3. Scheme of the interferometer setup (BS—beam splitter, CAM—high-speed camera, LAS—laser, FF—fiber ferrule, FS—fiber-splitter, L0, L1, L2—lenses).

3. Preliminary Results and Discussion

Initial measurements from previous experiments on stationary cascades have demonstrated the potential of the high-speed interferometric technique in capturing detailed flow structures, including shock waves and boundary layer interactions [1]. The current study extends this approach to oscillating blades. The recent measurements were carried out for two different inter blade phase angles (IBPA = ±90°) and three blade oscillation frequencies ($f_b = 50$, 100, and 150 Hz) with the oscillation amplitude set to 0.25°. Cycle-to-cycle repeatability is illustrated in Figure 4, where the ensemble average of 306 cycles at 150 Hz for blade deflection and pressure measured at one suction-surface location is presented. For each regime, a sequence in the length of several blade oscillation periods was captured using FASTCAM SA-Z 2100K M64GB monochrome high-speed camera sampling at 30 kHz. The resulting interferograms (Figure 5), showing the fringes representing the levels of the constant refractive index n, were evaluated using the Gladstone-Dale Equation (12) linking refractive index to density [25].

$$n - 1 = K\rho \quad (12)$$

Then, knowing the density $\rho(x, y)$ and the total density ρ_0 at the inlet, the distribution of the isentropic Mach number $M_{is}(x, y)$ can be easily obtained from the equation

$$M_{is} = \sqrt{\frac{2}{\gamma - 1}\left[\left(\frac{\rho}{\rho_0}\right)^{\gamma - 1} - 1\right]} \quad (13)$$

where γ is the heat capacity ratio [25].

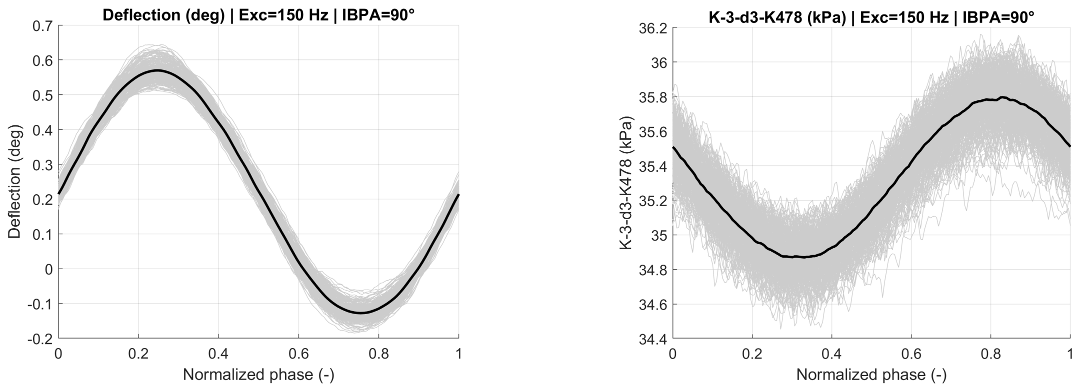

(**a**) (**b**)

Figure 4. Ensemble average of blade deflection (**a**) and surface pressure (**b**) together with all cycles used for averaging.

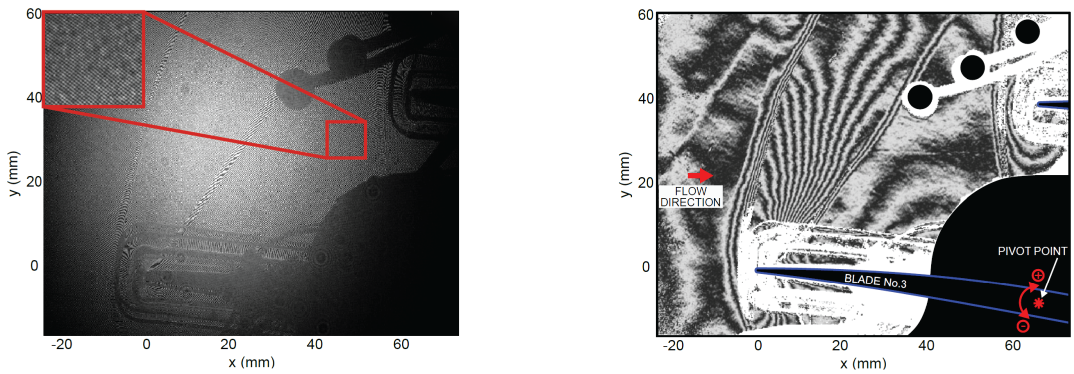

(**a**) (**b**)

Figure 5. Example interferogram obtained during the current measurements (**a**) and synthetic interferogram generated from the reconstructed phase distribution for qualitative visualization of the measured flow field (**b**). Regions without visible fringes correspond predominantly to areas shadowed by non-transparent objects inside the test section, such as the blades, pressure sensors, sensor wiring, and mechanical support structures. These regions were excluded from further evaluation.

The resulting distributions of isentropic Mach number near the middle blade (No. 3) are shown in Figures 6 and 7 for three selected regimes: (i) IBPA $= 90°$, $f_b = 50$ Hz; (ii) IBPA $= -90°$, $f_b = 50$ Hz; and (iii) IBPA $= 90°$, $f_b = 150$ Hz. For each regime, the snapshots correspond to the time instant when the middle blade is at either its maximum positive or negative deflection. In Figure 6a, the most prominent flow features are indicated, including bow shocks upstream of the blades and lip shocks originating at the junction between the rounded trailing edge and the blade surface.

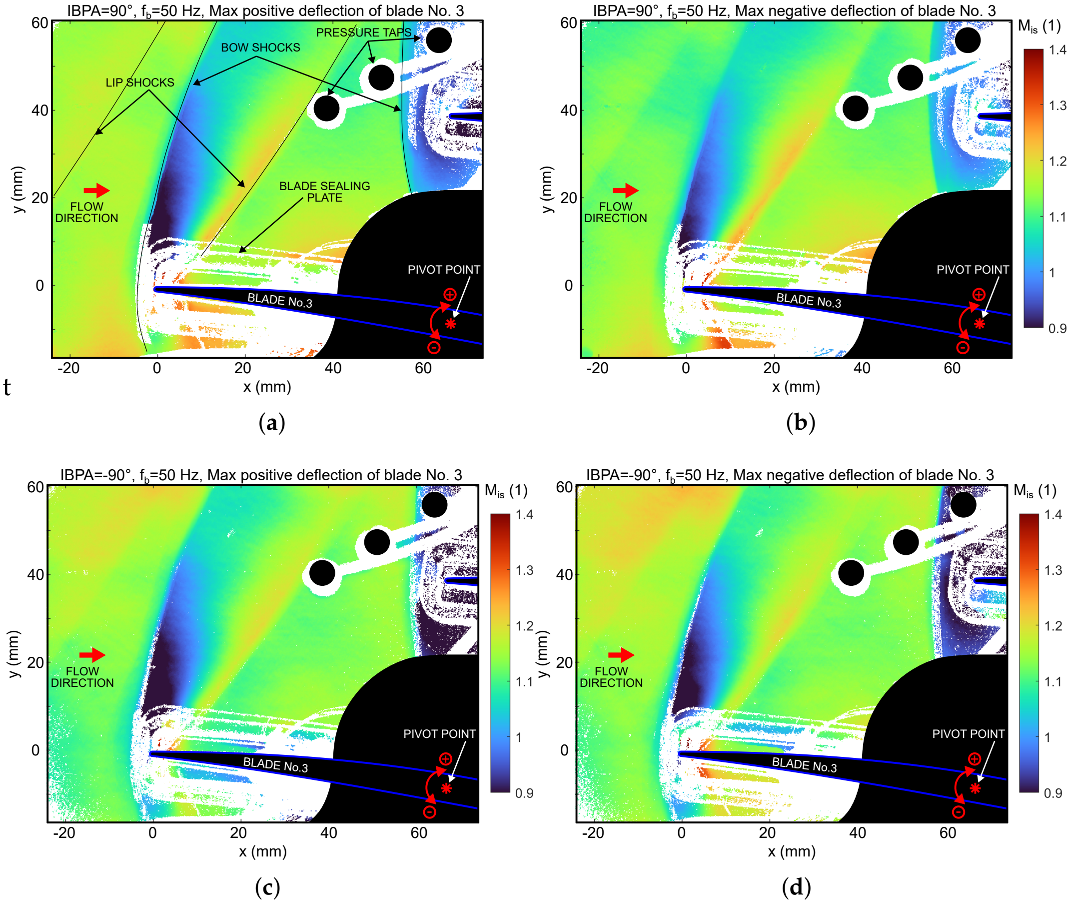

Figure 6. Resulting isentropic Mach number distributions M_{is} at the blade oscillation frequency $f_b = 50$ Hz: (**a**) max positive and (**b**) max negative deflection at IBPA $= 90°$; (**c**) max positive and (**d**) max negative deflection at IBPA $= -90°$.

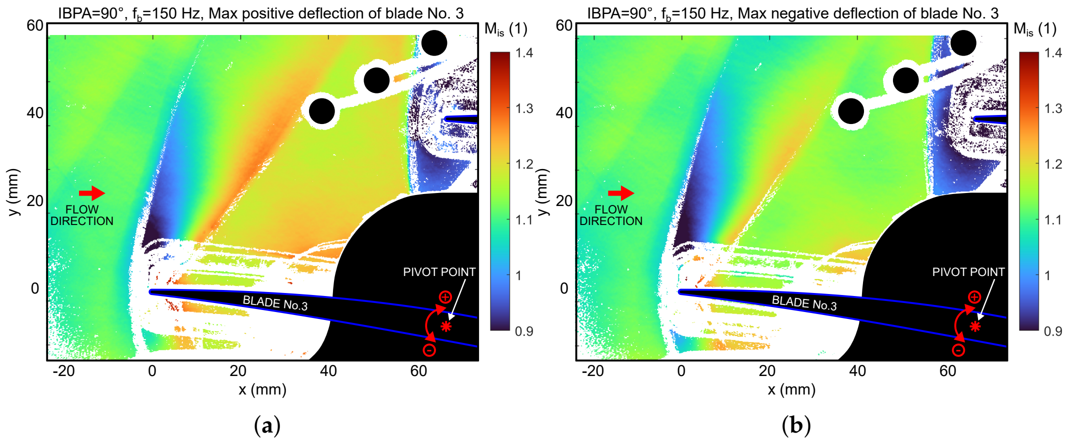

Figure 7. Resulting isentropic Mach number distributions M_{is} at the blade oscillation frequency $f_b = 150$ Hz: (**a**) max positive and (**b**) max negative deflection at IBPA $= 90°$.

Although only small differences are visible across these cases, the most dynamic effects occur on the pressure side of blade No. 3, where a small supersonic region, terminated by an oscillating normal shock, forms periodically. It can be observed that, for maximum negative deflection of the middle blade, a stronger expansion appears on the forward part of the pressure side compared with positive deflection. This is expected, as negative deflection reduces the incidence angle, allowing the expansion region to reach its maximum extent.

This effect is more pronounced for IBPA = 90°, as blade No. 2 (not visible) moves from its maximum positive deflection toward its neutral position. In contrast, for IBPA = −90°, blade No. 2 moves from its maximum negative deflection toward neutral, resulting in a more open inter-blade channel between blades No. 2 and 3 in this case.

The influence of oscillation frequency is illustrated in Figure 7, which shows the isentropic Mach number distribution for IBPA = 90° and $f_b = 150$ Hz. Again, the changes in shock position between limiting deflections are relatively small, but the movement is more pronounced than at $f_b = 50$ Hz. It is not clear whether this effect is due to flow phenomena or to increased blade deflection amplitude caused by elastic deformation during torsional oscillation. The laser triangulation sensor measured a mid-span deflection amplitude of approximately 0.32° for an excitation setting of 0.25° and frequency $f_b = 150$ Hz, while for $f_b = 50$ Hz, the measured mid-span deflection amplitude was 0.254°. The same difference in blade deflection has been observed also in cases with no flow (Figure 8).

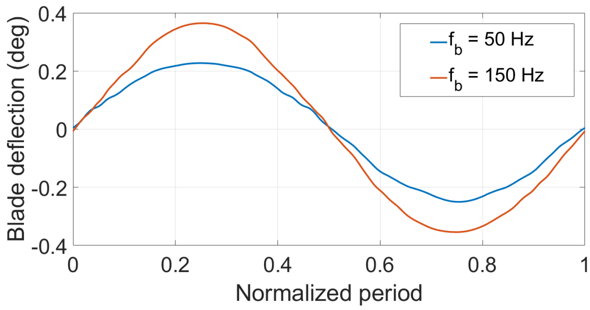

Figure 8. Ensemble average of blade deflection over one period at different excitation frequencies with flow off.

It should also be noted that the flow field might also changes between different periods; therefore, statistical evaluation is required to obtain representative data.

Effect of excitation frequency and IBPA on the blade suction side loading is shown in Figure 9 where distributions of pressure amplitude in terms of pressure coefficient and phase shift between pressure and blade motion are provided. Pressure amplitudes differ namely in the front half of the blade surface upstream the bow shock of blade number 2. Effect of this shock is apparent as a pressure amplitude peak close to x/c = 0.4. All measured pressures downstream of this point exhibit practically the same amplitude trends except for higher values in case of exc. frequency $f_b = 150$ Hz. In the front part, amplitudes are decreasing along the chord for the negative IBPA with overall maximum at the location of the first pressure tap. This is due to the influence of the blade 2 which leads the motion here. For positive IBPAs, this trend is opposite. Scattered amplitudes at the location of the first pressure tap illustrate significant effect of the strong expansion and subsequent lip shock just behind the leading edge on the loading of the blade front part.

The phase shift between pressure and blade motion at $f_b = 50$ Hz exhibits opposite trends for positive and negative IBPA, with different magnitudes. Signals are defined as in phase when the maximum blade displacement coincides with the minimum unsteady pressure; a positive phase shift indicates that the pressure leads the motion. The motion of the inner branch of the bow shock on blade 2 can be approximated using values at $x/c = 0.4$. For negative IBPA, the pressure leads the blade motion by 163°, indicating that the shock moves upstream with a slight lag when the blade pivots in the positive sense (i.e., when the leading edge moves upward). For positive IBPA, the shock moves downstream with the blade motion, but with a phase lag of 52°. Similarly, at $f_b = 150$ Hz and IBPA = 90°, the shock also moves downstream with the blade motion, but in this case it leads by 36°. The abrupt change in phase shift at the location of the first pressure tap for $f_b = 150$ Hz again confirms the significant effect of the strong expansion and the subsequent lip shock. However, the dynamic blade loading in the upstream region ahead of the first pressure tap can only be evaluated using the optical methods described in this paper. The evaluation of raw images, however, still requires optimization for batch processing.

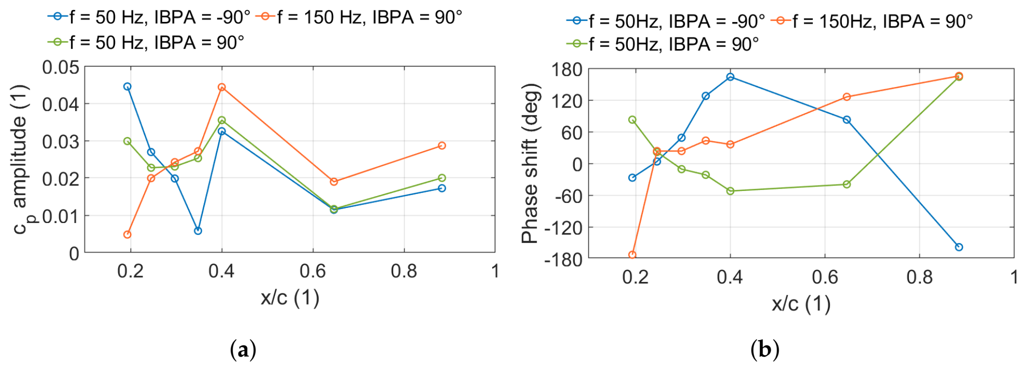

Figure 9. Cp amplitude (**a**) and phase shift between pressure and blade motion (**b**) distribution along the blade suction surface

4. Measurement Uncertainty Estimation

For flow measurements in wind tunnels, the refractive index along the interferometer optical axis is assumed to be constant, and the optical phase $\Delta\varphi'_{\lambda 2}$ can be related to the density distribution ρ using Equation (11), where $L_T = 160$ mm is the wind tunnel test-section width. This relation assumes a quasi-two-dimensional flow field. Deviations from this assumption, such as side-wall boundary layers, vortical structures, or local three-dimensional flow separation, may affect the phase integrated along the optical path and consequently distort the reconstructed density field. These effects were minimized by the design of the test section and supported by numerical simulations. In the present implementation, the phase reconstructed at the wavelength $\lambda_2 = 660$ nm was used as the quantitative measurement channel. The phase reconstructed at $\lambda_1 = 550$ nm was used only to generate the synthetic phase ϕ in Equation (2), corresponding to the synthetic wavelength $\Lambda \approx 3.3$ µm, according to Equation (3). The synthetic phase is required for the robust phase unwrapping described by Equation (10). Therefore, λ_1 does not directly enter the final density conversion. Its role is to support the determination of the correct fringe order of the λ_2-phase map. The final quantitative accuracy is mainly governed by the phase noise of the λ_2 channel, the test-section width L_T, the reference density, and the Gladstone–Dale constant. Quantitative interferometric measurements in an aerodynamic tunnel are affected by several uncertainty sources. The dominant contributions are the phase noise, estimated as $u_{\Delta\varphi} = 0.4$ rad, the effective uncertainty of the test-section width and optical path length, estimated as $u_{L_T} = 1$ mm, and the uncertainty of the reference density, estimated as $u_{\rho_0} = 2 \times 10^{-3}$ kg m^{-3}. Smaller contributions arise from the wavelength uncertainty of the measurement channel, estimated as $u_{\lambda_2} = 1$ nm, and from the uncertainty of the Gladstone–Dale constant, estimated as $u_K = 1 \times 10^{-6}$ m^3 kg^{-1}. The optical phase can be affected by non-uniform illumination, low-quality optical windows, imperfect object-to-reference beam intensity ratio, speckle-like disturbances, diffraction from dust particles or sharp edges, and electronic noise. Environmental disturbances, such as vibrations and air turbulence outside the test section, are largely suppressed by the short camera exposure time. Nevertheless, residual phase distortions may occur between the reference and flow-on frames. Additional uncertainty is related to the assumption that the light propagates through a constant refractive-index distribution along the optical path. This assumption can be violated by local three-dimensional flow structures, side-wall effects, inaccurate alignment of the illumination beam, and ray bending caused by strong refractive-index gradients. If the object beam is not perpendicular to the test section, the effective optical path length increases approximately as $1/\cos\alpha$, where α is the misalignment angle, and the measured information is also displaced laterally. The alignment was therefore performed carefully by observing blade edges and their shadows so that the object beam was coincident with the blade edge. Even in a well-aligned configuration, ray bending in regions with strong density gradients may cause a local geometric displacement of the reconstructed information. This displacement was estimated to be on the order of few pixels in the regions with the largest gradients and negligible elsewhere. The density uncertainty $u_\rho \approx 0.005\ \mathrm{kg\,m^{-3}}$ was evaluated from Equation (11) as

$$u_\rho = \left[\left(\frac{\partial\rho}{\partial\lambda_2}u_{\lambda_2}\right)^2 + \left(\frac{\partial\rho}{\partial\varphi}u_{\Delta\varphi}\right)^2 + \left(\frac{\partial\rho}{\partial K}u_K\right)^2 + \left(\frac{\partial\rho}{\partial L_T}u_{L_T}\right)^2 + \left(\frac{\partial\rho}{\partial\rho_0}u_{\rho_0}\right)^2\right]^{1/2}. \quad (14)$$

The most significant contributions are the phase noise, the effective optical path-length uncertainty, and the reference-density uncertainty, while the wavelength and Gladstone–Dale constant contributions are at least one order of magnitude smaller. The density uncertainty was further propagated to the isentropic Mach number using Equation (13). Including the uncertainty of the total density, estimated as $1 \times 10^{-3}\ \mathrm{kg\,m^{-3}}$, and the uncertainty of the heat capacity ratio, estimated as 5×10^{-3}, gives a Mach-number relative uncertainty of about 0.5%. The role of the auxiliary wavelength λ_1 must be interpreted separately from the density uncertainty. Its uncertainty affects the reliability of the phase-unwrapping procedure rather than the final density conversion. In the standard two-wavelength approach, an incorrect fringe order is obtained if the error in the phase-difference quantity Ω exceeds one half of the 2π interval $|\varepsilon(\Omega)| < \pi$. In the robust unwrapping approach used here, this requirement is relaxed. Since the wrapped phase difference Ω_W is spatially unwrapped, the relevant condition is not the absolute phase error itself, but the local phase-gradient error $|\nabla\varepsilon(\Omega_W)| < \pi$. Provided that this condition is satisfied, the auxiliary wavelength only supports the determination of the correct fringe order and does not limit the final quantitative accuracy in the same way as the measurement wavelength. If the condition is violated locally, the resulting error is not a small continuous measurement uncertainty but a fringe-order error, producing a phase jump of an integer multiple of 2π. Such regions must therefore be treated as local unwrapping failures.

5. Conclusions and Limitations

In conclusion, the high-speed two-wavelength interferometric method has demonstrated a robust capability to resolve intricate unsteady flow patterns and transient shock-wave oscillations under active blade flutter conditions. The primary technical advantage of this methodology lies in its low demands on the optical window quality, enabling full-field flow quantification through organic-glass side walls. This capability establishes a crucial baseline for future compressor cascade investigations, where complex suction slots must be cut directly into the windows to maintain a representative Axial Velocity Density Ratio (AVDR). Present operational limitations include a restricted field of view and compromised visibility directly adjacent to the blade surfaces, primarily caused by rapid mechanical wear of the organic-glass sealing plates required for the oscillating blade mechanism. Consequently, future work will focus on expanding the optical field of view to capture a larger portion of the cascade, as well as conducting complementary stationary blade investigations to decouple spontaneous shock oscillations from forced blade motions. Ultimately, while comprehensive integration of these optical fields with unsteady surface pressure data is ongoing, these initial quantitative measurements contribute valuable insights into transonic flutter phenomena and provide high-fidelity validation data for advanced computational fluid dynamics (CFD) codes.

Author Contributions: Conceptualization, J.H. and P.P.; Methodology P.P., J.H. and D.Š.; investigation, J.H., P.P. and D.Š.; writing—original draft preparation, J.H. and P.P.; writing—review and editing, P.P. and D.Š. and J.L.; supervision, D.Š. and J.L. All authors have read and agreed to the published version of the manuscript.

Funding: This research was supported by the Ministry of Education Youth and Sports of the Czech Republic under the grant LUAUS23231, Origins and mechanisms of flutter and non-synchronous vibration in modern turbomachines operating at wide range of regimes. Institutional support RVO 61388998 is also gratefully acknowledged.

Data Availability Statement: The data presented in this study are available on request from the corresponding author.

Conflicts of Interest: The authors declare no conflicts of interest. The funders had no role in the design of the study; in the collection, analyses, or interpretation of data; in the writing of the manuscript; or in the decision to publish the results.

Abbreviations

The following abbreviations and symbols are used in this manuscript:

AVDR	Axial Velocity Density Ratio
DFVLR	German Test and Research Institute for Aviation and Space Flight
IBPA	Inter Blade Phase Angle
MCA	Multi Circular Arc
α_b	amplitude of the blade oscillation motion
γ	specific heat ratio
ρ	density
f_b	blade oscillation frequency
K	Gladstone-Dale constant
M_{is}	isentropic Mach number
n	refractive index
p	pressure
subscript 0	total conditions
subscript 1	cascade inlet conditions

References

1. Šimurda, D.; Psota, P.; Šidlof, P.; Kielb, R.; Luxa, M.; Hála, J.; Lepicovsky, J. Optical measurement and visualization of transonic airflow in a compressor blade cascade. *J. Vis.* **2023**, *26*, 529–549. [CrossRef]
2. Liu, N.; Ma, L. Regularized tomographic PIV for incompressible flows based on conservation of mass. *Appl. Opt.* **2020**, *59*, 1667–1677. [CrossRef]
3. Scarano, F. Tomographic PIV: Principles and practice. *Meas. Sci. Technol.* **2012**, *24*, 012001. [CrossRef]
4. Li, G.; Kontis, K.; Fan, Z. Automatic Shock Detection, Extraction, and Fitting in Schlieren and Shadowgraph Visualization. *AIAA J.* **2021**, *59*, 2312–2317. [CrossRef]
5. Erdem, E.; Kontis, K. Experimental Investigation of Sonic Transverse Jets in Mach 5 Crossflow. *Aerosp. Sci. Technol.* **2021**, *110*, 106419. [CrossRef]
6. Biasiori-Poulanges, L.; El-Rabii, H. High-magnification shadowgraphy for the study of drop breakup in a high-speed gas flow. *Opt. Lett.* **2019**, *44*, 5884–5887. [CrossRef] [PubMed]
7. Mann, C.J.; Yu, L.F.; Lo, C.M.; Kim, M.K. High-resolution quantitative phase-contrast microscopy by digital holography. *Opt. Express* **2005**, *13*, 8693–8698. [CrossRef]
8. Yamaguchi, I.; Ida, T.; Yokota, M.; Yamashita, K. Surface shape measurement by phase-shifting digital holography with a wavelength shift. *Appl. Opt.* **2006**, *45*, 7610–7616. [CrossRef]
9. Di, J.L.; Zhang, J.W.; Xi, T.L.; Ma, C.J.; Zhao, J.L. Improvement of measurement accuracy in digital holographic microscopy by using dual-wavelength technique. *J. Micro-Nanolithogr. Mems Moems* **2015**, *14*, 1932–5134. [CrossRef]
10. Parshall, D.; Kim, M.K. Digital holographic microscopy with dual-wavelength phase unwrapping. *Appl. Opt.* **2006**, *45*, 451–459. [CrossRef]

11. Khmaladze, A.; Kim, M.; Lo, C.M. Phase imaging of cells by simultaneous dual-wavelength reflection digital holography. *Opt. Express* **2008**, *16*, 10900–10911. [CrossRef]
12. Kuhn, J.; Colomb, T.; Montfort, F.; Charriere, F.; Emery, Y.; Cuche, E.; Marquet, P.; Depeursinge, C. Real-time dual-wavelength digital holographic microscopy with a single hologram acquisition. *Opt. Express* **2007**, *15*, 7231–7242. [CrossRef] [PubMed]
13. Turko, N.A.; Shaked, N.T. Simultaneous two-wavelength phase unwrapping using an external module for multiplexing off-axis holography. *Opt. Lett.* **2017**, *42*, 73–76. [CrossRef]
14. Guo, R.L.; Zhang, W.G.; Liu, R.; Duan, C.L.; Wang, F. Phase unwrapping in dual-wavelength digital holographic microscopy with total variation regularization. *Opt. Lett.* **2018**, *43*, 3449–3452. [CrossRef]
15. Jaedicke, V.; Goebel, S.; Koukourakis, N.; Gerhardt, N.C.; Welp, H.; Hofmann, M.R. Multiwavelength phase unwrapping and aberration correction using depth filtered digital holography. *Opt. Lett.* **2014**, *39*, 4160–4163. [CrossRef] [PubMed]
16. Meiners-Hagen, K.; Schodel, R.; Pollinger, F.; Abou-Zeid, A. Multi-Wavelength Interferometry for Length Measurements Using Diode Lasers. *Meas. Sci. Rev.* **2009**, *9*, 16–26. [CrossRef]
17. Turko, N.A.; Eravuchira, P.J.; Barnea, I.; Shaked, N.T. Simultaneous three-wavelength unwrapping using external digital holographic multiplexing module. *Opt. Lett.* **2018**, *43*, 1943–1946. [CrossRef] [PubMed]
18. Lepicovsky, J.; Simurda, D.; Sidlof, P.; Luxa, M. Exploratory Experiments for Simple Approximation of Blade Flutter Aerodynamic Loading Function. In *ASME Turbo Expo 2022: Turbomachinery Technical Conference and Exposition. Volume 8A: Structures and Dynamics—Aerodynamics Excitation and Damping; Bearing and Seal Dynamics; Emerging Methods in Engineering Design, Analysis, and Additive Manufacturing; Fatigue, Fracture, and Life Prediction*; ASME: New York, NY, USA, 2022; p. V08AT21A023. [CrossRef]
19. Lepicovsky, J.; Šimurda, D.; Kielb, R.E.; Šidlof, P.; Štěpán, M. Quasi-Dynamic Approximation of Unsteady Pressure Distribution for Transonic Airfoils in Flutter. *J. Turbomach.* **2023**, *145*, 081010. [CrossRef]
20. Schreiber, H.A.; Starken, H. Experimental Cascade Analysis of a Transonic Compressor Rotor Blade Section. *J. Eng. Gas Turbines Power* **1984**, *106*, 288–294. [CrossRef]
21. Psota, P.; Çubreli, G.; Šimurda, D.; Šidlof, P.; Kredba, J.; Stašík, M.; Lédl, V. Noise-resistant two-wavelength interferometry for single-shot measurement of high-gradient flows. *Opt. Lasers Eng.* **2023**, *164*, 107505. [CrossRef]
22. Merzkirch, W. *Flow Visualization*, 2nd ed.; Academic Press: New York, NY, USA, 1987.
23. Psota, P.; Çubreli, G.; Hála, J.; Šimurda, D.; Šidlof, P.; Kredba, J.; Stašík, M.; Lédl, V.; Jiránek, M.; Luxa, M.; et al. Characterization of Supersonic Compressible Fluid Flow Using High-Speed Interferometry. *Sensors* **2021**, *21*, 8158. [CrossRef]
24. Psota, P.; Stašík, M.; Jiránek, M.; Lédl, V.; Hála, J. Three-dimensional temperature measurement in harsh environments using quadriwave lateral shearing interferometric tomography. *Opt. Lasers Eng.* **2025**, *184*, 108566. [CrossRef]
25. Shapiro, A.H. *The Dynamics and Thermodynamics of Compressible Fluid Flow*; Ronald Press: New York, NY, USA, 1953; Volume 1.